Advanced Materials

ADVANCED MATERIALS
www.advmat.de

RESEARCH ARTICLE OPEN ACCESS

From Thin Films to Nanodots: Bottom-Up Integration of Fe_3O_4 on Nb:STO for Functional Oxide Nanostructures

Yifan Xu[1,2] | Connie Bednarski-Meinke[2] | Yen-Po Liu[3] | Erkai Wang[3] | Asma Qdemat[2,4] | Peijia Yuan[3] | Lilian Maria Vogl[5] | Patrick Schöffmann[6] | Thomas Saerbeck[7] | Chenyang Yin[1,2] | Gerhard Dehm[5] | Felix Gunkel[3] | Regina Dittmann[3] | Oleg Petracic[2,1] | Mai Hussein Hamed[2,8]

[1]Heinrich Heine Universität Düsseldorf, Fakultät für Mathematik und Naturwissenschaften, Düsseldorf, Germany | [2]Jülich Centre for Neutron Science (JCNS-2), JARA-FIT, Forschungszentrum Jülich GmbH, Jülich, Germany | [3]Peter Grünberg Institute (PGI-7), Forschungszentrum Jülich GmbH, Jülich, Germany | [4]Oak Ridge National Laboratory, Oak Ridge, USA | [5]Max Planck Institute for Sustainable Materials, Düsseldorf, Germany | [6]Synchrotron SOLEIL, L'Orme des Merisiers, Saint-Aubin, France | [7]Institut Laue-Langevin, Grenoble Cedex 9, France | [8]Helwan University, College of Science, Cairo, Egypt

Correspondence: Yifan Xu (yi.xu@fz-juelich.de) | Connie Bednarski-Meinke (c.bednarski-meinke@fz-juelich.de) | Mai Hussein Hamed (Mai.hussein@science.helwan.edu.eg)

Received: 12 September 2025 | **Revised:** 17 November 2025

Keywords: AAO membrane | c-AFM | Fe_3O_4 | nanodots | resistive switching

ABSTRACT

Epitaxial heterostructures of iron oxide thin films on oxide substrates are promising for spintronic applications. Scaling down such heterostructures into ordered nanostructures enables integration into functional devices. However, fabricating well-ordered nanostructures while retaining their structural and functional integrity remains challenging. A bottom-up approach is used to grow epitaxial Fe_3O_4 nanodot arrays on Nb-doped $SrTiO_3$(Nb:STO) substrates integrating anodic aluminum oxide (AAO) templates combined with pulsed laser deposition. Following this method, the lateral confinement of Fe_3O_4 into 30 and 70 nm nanodots with 3D long-range ordering is then confirmed by grazing-incidence small-angle X-ray scattering (GISAXS) and scanning electron microscopy (SEM). Building on this structural evidence, the Verwey transition is found to be retained, as observed in the continuous film. To explore its applicability in nanoelectronics, conductive atomic force microscopy (c-AFM) is used to probe local electrical behavior, and reveals bipolar resistive switching at room temperature in individual nanodots, consistent with behavior observed in thin films. Together, these results establish the first demonstration of ordered epitaxial Fe_3O_4/Nb:STO nanodots with preserved structural, magnetic, and electrical functionalities, providing a generalizable route for nanoscale integration of complex oxides.

1 | Introduction

Transition metal oxides with strongly coupled charge, spin, and orbital degrees of freedom are of great interest for both fundamental research and functional applications [1–3]. Among these, Fe_3O_4 (magnetite) stands out for its high Curie temperature (860 K), electronic conductivity, and sensitivity to oxygen stoichiometry. A key feature of Fe_3O_4 is its ability to undergo topotactic transitions to/from FeO or γ-Fe_2O_3 by controlled oxidation or reduction, which allows reversible tuning of its magnetic and electronic properties while often preserving crystallographic orientation relationships [4–8]. Fe_3O_4 and γ-Fe_2O_3 are functionally distinct: Fe_3O_4 is a mixed-valence conductor with high saturation magnetization [9, 10], while γ-Fe_2O_3 is a ferrimagnetic insulator with a significantly larger bandgap, resulting from its fully oxidized Fe $^{3+}$ state and the presence of cation vacancies [11]. The transition between these phases is particularly interesting for tunable oxide electronics, as it allows control over electronic and magnetic states. Both adopt a spinel-type structure (space group $Fd\bar{3}m$) and exhibit nearly identical cubic lattice parameters (8.392 Å for Fe_3O_4 [12] and 8.362 Å for γ-Fe_2O_3 [13]), with only subtle differences in Fe site occupancy. These structural similarities make distinguishing between them using standard laboratory X-ray diffraction difficult. While this complicates experimental identification, it also enables topotactic phase transformations with minimal lattice distortion. This is advantageous for designing reversible, low-strain switching elements in functional oxide systems [14, 15].

Although high-quality Fe_3O_4 thin films have been extensively studied, transferring their structural and functional properties to ordered nanoscale architectures remains challenging [16, 17]. Integrating epitaxial oxide nanostructures into scalable patterns requires not only the preservation of crystalline quality, but also precise control over stoichiometry, magnetic ordering, and interfacial structure. This is particularly important for magnetite, as small deviations in oxygen content, cation distribution, or lattice strain can significantly alter both electronic transport and magnetic behavior [18, 19]. Previous attempts to scale Fe_3O_4 into patterned nanostructures using top-down or self-assembly techniques have often resulted in compromised crystalline quality, non-uniform stoichiometry, or degraded magnetic performance [20–22]. This highlights the need for improved methods that preserve properties of Fe_3O_4 at the nanoscale.

To address these challenges, bottom-up approaches such as template-assisted growth have attracted attention as alternatives to conventional lithographic methods [23, 24]. Among these, anodic aluminum oxide (AAO) templates provide a simple and cost-effective route to highly ordered nanostructures with lateral feature sizes down to a few tens of nanometers. While AAO-based nanostructuring has been widely applied to polycrystalline metal oxides [25, 26], its use in structurally ordered, functionally active oxide systems remains limited.

Although template-assisted growth enables lateral patterning, substrate choice and interface engineering remain critical for maintaining epitaxial quality and functional properties [27]. Nb-doped $SrTiO_3$ (Nb:STO) not only provides a conductive bottom electrode but also acts as an active substrate, with tunable surface chemistry and oxygen exchange properties [28–30]. However, issues such as the -7.5% lattice mismatch between Fe_3O_4 and STO, or the formation of interfacial oxides, make it difficult to grow atomically sharp and stoichiometric interfaces [31, 32].

We employ a bottom-up strategy to fabricate epitaxial Fe_3O_4 nanodots on Nb:STO using commercial AAO templates and pulsed laser deposition (PLD). Starting with epitaxially grown Fe_3O_4 thin films, we examine the interface oxygen stoichiometry and phase composition. To accomplish this, we use transmission electron microscopy (TEM), X-ray magnetic circular dichroism (XMCD), and polarized neutron reflectometry (PNR). Next, we scale down the system into nanodot arrays and characterize the ordering using scanning electron microscopy (SEM) and grazing-incidence small-angle X-ray scattering (GISAXS). A key question, we address is whether the film's main features — crystallinity, magnetism, and stoichiometry—are preserved at the nanoscale. Moreover, conductive atomic force microscopy (cAFM) measurements reveal local conductivity changes under applied bias, further suggesting that Fe_3O_4 nanodots could be used to explore electrically tunable behavior, which has potential applications in future devices [33].

Overall, our work demonstrates a scalable method for patterning oxide nanostructures that preserves epitaxial and magnetic qualities. It also provides a platform to study nanoscale interface effects and functional properties in confined geometries [34–36].

2 | Results and Discussion

2.1 | Characterization of Fe_3O_4/Nb:STO Thin Films: Interface, Structure, and Magnetic Properties

Growing high quality Fe_3O_4 films on STO has multiple challenges: non-epitaxy [31], high density of dislocations [32], or interfacial layers of FeO [37] or γ-Fe_2O_3 phase [38]. Despite these challenges, we here demonstrate growth of high-quality Fe_3O_4 films on Nb:STO. AFM confirms the smooth surface morphology of the Fe_3O_4 film with a root-mean-square (RMS) surface roughness of 0.45 nm, as detailed in Section S1, while XRD confirms the out-of-plane (001) orientation on Nb:STO (001) as detailed in Section S2. However, with AFM and XRD, we cannot probe the oxidation state of the interface. Therefore, we performed STEM, XMCD, and PNR measurements.

To gain atomic-level insight into the film quality and its interface with the STO substrate, high-angle annular dark field (HAADF) scanning transmission electron microscopy (STEM) imaging was performed. Figure 1a shows a HAADF-STEM image of the Fe_3O_4 (001) thin film grown on a Nb:STO(001) substrate. The image reveals well-aligned atomic columns throughout the film, indicating high crystalline quality. The brighter atomic columns, corresponding to Fe, Sr, and Ti due to their higher atomic numbers, are clearly distinguished from the dimmer O columns. The thin film layer exhibits a highly ordered structure, and a representative unit cell of an inverse spinel lattice is highlighted in the magnified region. This structure is consistent with Fe_3O_4, where anti-phase boundaries are frequently reported as characteristic defects in epitaxial films [39, 40]. In addition, the presence of nanometer-sized γ-Fe_2O_3 regions cannot be fully excluded due to structural similarities.

The selected area electron diffraction pattern (see details in Section S3) reveals that the Fe_3O_4 is relaxed with respect to the Nb:STO, consistent with a lattice mismatch of around 7.5%. The darker contrast region of approximately 1 nm at the interface in Figure 1a likely reflects a strained interfacial layer, which could arise from misfit dislocations or gradual strain relaxation across the interface. A low-magnification TEM image is shown in Section S4.

To further investigate the origin of the darker contrast observed at the Fe_3O_4/Nb:STO interface, energy-dispersive X-ray spectroscopy (EDS) mapping was performed, as shown in Figure 1b. The corresponding elemental mapping result is provided in Figure S3c for reference. The EDS elemental maps show a homogeneous distribution of Fe and O throughout the film and no evidence of elemental intermixing between the film and the substrate. In particular, no diffusion of substrate elements

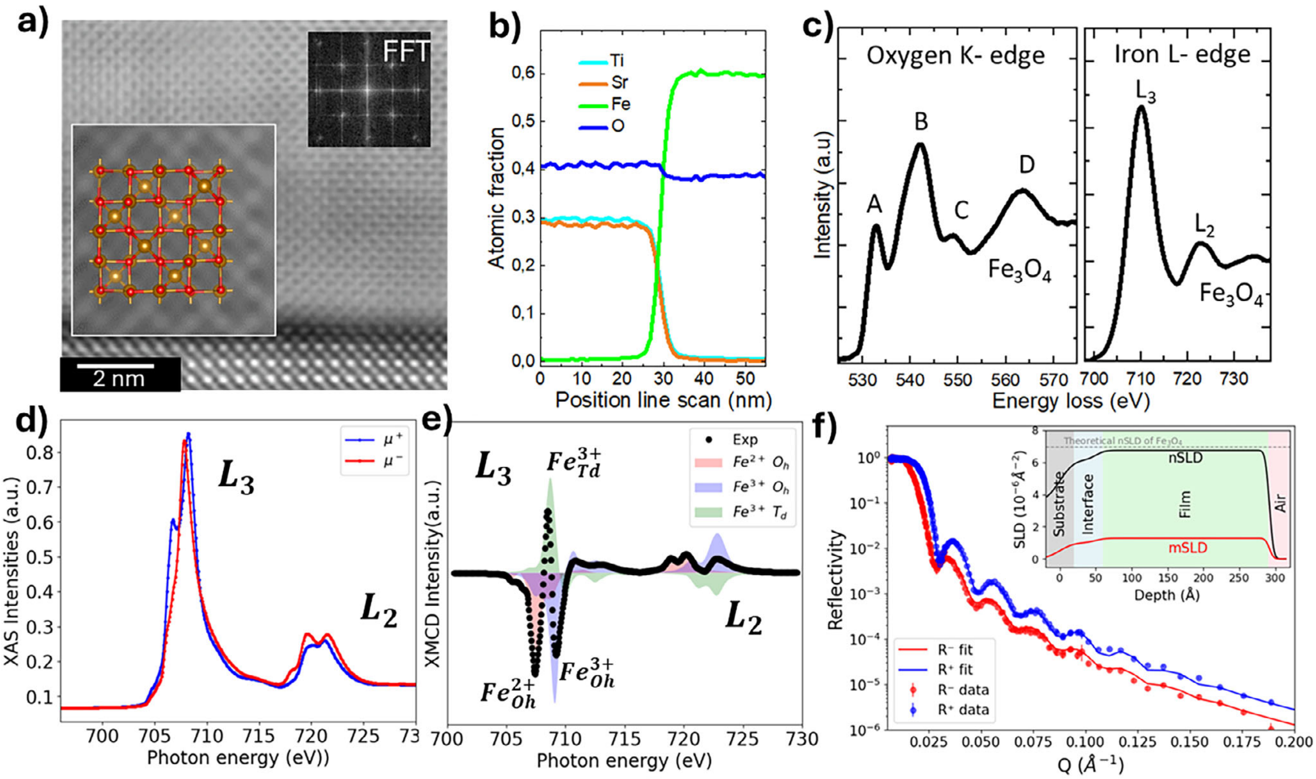

FIGURE 1 | (a) High-resolution STEM-HAADF image of a Fe_3O_4 (001) thin film grown on a Nb:STO(001) substrate. The Fe_3O_4 lattice is highlighted in the zoomed-in inset. (b) EDS line profile across the film–substrate interface. The corresponding mapping result is shown in Figure S3c. Electron Energy Loss Spectroscopy (EELS) spectra of the iron oxide thin film at (c) the Fe $L_{2,3}$-edge and the O K-edge. (d) Fe $L_{2,3}$-edge XAS spectrum of a 30 nm Fe_3O_4 thin film measured at room temperature under a 50 mT magnetic field. (e) Corresponding XMCD spectrum, with experimental data fitted to simulate contributions from Fe ions at different lattice sites. (f) Polarized neutron reflectivity (PNR) data (dots) and corresponding fits (solid lines) obtained using GenX with the inset of Nuclear and magnetic scattering length density (NSLD and MSLD) profiles derived from the PNR fits.

(Sr or Ti) into the Fe_3O_4 layer is observed. Thus, the contrast cannot be attributed to cation intermixing, although oxygen exchange cannot be excluded given the limited sensitivity of EDS to light elements [41]. An overview HAADF image with the corresponding region selected for EDS line scans, along with elemental maps of Sr, Ti, O, and Fe, is provided in the Section S3.

Due to their structural similarities, the phases of Fe_3O_4 and γ-Fe_2O_3 cannot be distinguished by TEM imaging or diffraction alone. To resolve this issue, Electron Energy Loss Spectroscopy (EELS) was employed to obtain chemical information. Figure 1c shows the EELS data acquired at the O K-edge and the Fe L-edge. The Fe L-edge spectra display two well-defined peaks at 710 and 723 eV, which correspond to the L_3 and L_2 transitions from Fe 2p $_{3/2}$ and 2p $_{1/2}$ to unoccupied 3d states [42]. Across the series from FeO to α-Fe_2O_3, the peaks shift slightly toward higher energies, accompanied by an increase in the L_2/L_3 intensity ratio [42, 43]. The measured L_2/L_3 ratio of 5.1 falls within the reported range for Fe_3O_4 [42, 44]. This supports the assignment of the film to this phase. For the O K-edge, four characteristic peaks (A–D) can be identified. The measured A/B ratio of 0.63 is close to the reported value for Fe_3O_4 (0.69), confirming that the film corresponds predominantly to the Fe_3O_4 phase.

The slightly lower A/B intensity ratio compared to the reference suggests an increased defect density or slight changes in the oxygen content.

Taken together, the TEM, EDS, and EELS results suggest that the film is a relaxed Fe_3O_4 thin layer with an interface region that accommodates the mismatch via misfit dislocations or an interface reconstruction. There is no evidence of FeO formation or significant intermixing at the interface. To distinguish Fe_3O_4 from possible γ-Fe_2O_3 contributions and more accurately assess the film stoichiometry, X-ray absorption spectroscopy (XAS) and X-ray magnetic circular dichroism (XMCD) measurements were conducted at the Fe $L_{2,3}$-edge.

Figure 1d shows the Fe $L_{2,3}$-edge XAS spectrum for a 30 nm Fe_3O_4 thin film measured at room temperature under a 50 mT magnetic field, which displays a clear pre-edge feature typical of the mixed-valence state in Fe_3O_4. In Figure 1e, the XMCD spectrum exhibits a characteristic W shape—a known fingerprint of Fe_3O_4 [45]. A stoichiometric Fe_3O_4 bulk sample has intensity ratio between the main XMCD peaks (associated with the ferromagnetically coupled Fe $^{2+}_{Oh}$ and Fe $^{3+}_{Oh}$ sites) around 1.5 [38, 46]. In contrast, γ-Fe_2O_3 exhibits a significantly lower ratio of about 0.4 due to the absence of Fe $^{2+}$ ions [46]. In our film, this ratio is approximately 1.23, which deviates slightly from that of bulk magnetite. To quantify the iron site occupancy and the relative proportions of Fe_3O_4 and γ-Fe_2O_3 phases, the XMCD spectrum was quantitatively analyzed by fitting it as a linear combination of reference spectra corresponding to Fe^{2+}_{Oh}, Fe^{3+}_{Oh}, Fe^{3+}_{Td} sites. These model spectra were calculated using the CTM4XAS 5.5 software [47], with parameter sets adopted from Ref. [48]. The resulting ratios of Fe ions at these sites were determined as Fe^{3+}_{Td} : Fe^{2+}_{Oh} : Fe^{3+}_{Oh} = 33:25:42.

Assuming a homogeneous composition across the film, the oxidized magnetite phase $Fe_{3-\delta}O_4$ can be described by the formula:

$$Fe^{3+}[Fe^{2+}_{1-3\delta}Fe^{3+}_{1+2\delta}X_{\delta}]O_4$$

where X_δ denotes cation vacancies at octahedral sites and the bracket groups the octahedral-site cations [49]. Here, δ ranges from 0 (stoichiometric Fe_3O_4) to 0.33 (fully oxidized defect spinel γ-Fe_2O_3) [49].

The Fe^{2+}/Fe^{3+} ratio derived from XMCD fitting is: $\frac{Fe^{2+}}{Fe^{3+}} = \frac{25}{33+42} = \frac{25}{75}$. This value can be related to the vacancy parameter δ through the equation:

$$\frac{Fe^{2+}}{Fe^{3+}} = \frac{1-3\delta}{1+(1+2\delta)} \tag{1}$$

Solving for δ yields $\delta \approx 0.09$.

To further interpret the extracted δ value, we estimated the relative proportions of stoichiometric Fe_3O_4 and γ-Fe_2O_3 that would correspond to the observed composition. Assuming the film is composed of a mixture of these two phases with volume fractions x and $1-x$, respectively, the average composition satisfies:

$$x\,Fe_3O_4 + (1-x)\,\gamma\text{-}Fe_2O_3 = Fe_{3-\delta}O_4 \tag{2}$$

Substituting $\delta = 0.09$ gives:

$$3x + 2(1-x) = 3 - \delta \quad \Rightarrow \quad x = 1 - \delta = 0.91$$

This indicates that the film composition corresponds to approximately 91% Fe_3O_4 and 9% γ-Fe_2O_3 by volume.

This analysis provides a quantitative estimate of the overall Fe_3O_4 and γ-Fe_2O_3 phase fractions in the film. Although XAS and XMCD provide information about the average volume composition, they do not offer spatial resolution across the film's thickness. To investigate the distribution of iron oxide phases throughout the depth of the film, particularly at the interfaces, polarized neutron reflectometry (PNR) was employed. PNR is sensitive to both nuclear and magnetic depth profiles, complimenting X-ray-based methods by revealing potential variations in oxygen content and magnetic ordering across the layered structure [50, 51].

Neutron reflectivity data were collected at room temperature in a 1 T in-plane magnetic field and were fit using GenX [52]. Figure 1f shows the measured PNR data, with clear oscillations extending up to $Q = 0.12$ Å^{-1}, indicating the high structural quality and smooth interfaces of the thin film. The fitted nuclear scattering length density (nSLD) profile, shown in the inset of Figure 1f, reveals that the top layer of Fe_3O_4 has an nSLD of 6.98×10^{-6} Å^{-2} and a saturation magnetization of 3.39 μB/f.u., which are both in good agreement with reported bulk values for stoichiometric magnetite ($nSLD_{Fe_3O_4} = 6.97 \times 10^{-6}$ Å^{-2} [53], M_S = 3–4 μB/f.u. [54, 55]). In order to achieve a good fit to the PNR data, a thinner interfacial layer with a slightly reduced nSLD of 6.85×10^{-6} Å^{-2} was introduced, suggesting a deviation from ideal magnetite composition. The saturation magnetization in this region is 2.09 μB/f.u. (from the GenX fit), indicating a change in the oxidation state at the interface.

The interfacial layer is 3.0 ± 0.7 nm thick and is located between the Nb:STO substrate and the 26.9 ± 0.7 nm thick Fe_3O_4 film. The interfacial layer corresponds to approximately 10% of the total film thickness. This value closely matches the ≈9% γ-Fe_2O_3 fraction derived independently from XMCD analysis. Taken together, these results confirm that the oxidized γ-Fe_2O_3 phase is confined near the film–substrate interface, rather than distributed throughout the film. In the PNR fit, the transition at the interface appears gradual rather than abrupt. Since the HAADF-STEM image shows a clean, well-aligned interface, the broad SLD profile is unlikely to be caused by roughness at the interface. Rather, it may reflect a combination of chemical intermixing and strain relaxation near the interface, which can gradually affect the local composition or density over a few nanometers.

Based on the results from PNR, HAADF-STEM, EDS, and XMCD, the film can be described as a near-stoichiometric Fe_3O_4 layer with a partially oxidized interfacial region that is consistent with γ-Fe_2O_3. XMCD analysis yields $\delta \approx 0.9$ for $Fe_{3-\delta}O_4$, and the persistence of the Verwey transition confirms the presence of a near-stoichiometric Fe_3O_4 bulk phase. PNR corroborates this finding by revealing a layered structure with a γ-Fe_2O_3–rich interface. These observations are consistent with our previous report on Fe_3O_4/Nb:STO heterostructures using Hard X-ray Photoelectron Spectroscopy (HAXPES) and XMCD [38]. Together, these results demonstrate that a high-quality magnetite film with near-bulk magnetization and a defined substrate interface was successfully grown, offering a solid basis for fabricating well-controlled nanostructures.

2.2 | From Thin Film to Nanodots: Morphology and Ordering

After successfully growing high-quality Fe_3O_4 thin films, we fabricated laterally confined nanodots to study the effect of nanoscale geometry on their structural, magnetic, and electrical properties. Even subtle variations in ordering or size reduction are expected to influence these functional properties [56, 57], making it essential to first establish uniform, long-range ordered nanodot arrays.

Figure 2a–c illustrates the fabrication process for Fe_3O_4 nanodots using AAO templates. First, an AAO membrane is transferred onto the Nb:STO substrate (Figure 2a). Then, Fe_3O_4 is deposited (Figure 2b). The AAO serves as a physical mask during this step. After removing the template with Kapton tape, a well-ordered array of nanodots is obtained (Figure 2c). To study the impact of lateral confinement at different length scales, two sets of nanodot arrays were fabricated using AAO templates with average pore diameters of approximately 30 and 70 nm, respectively.

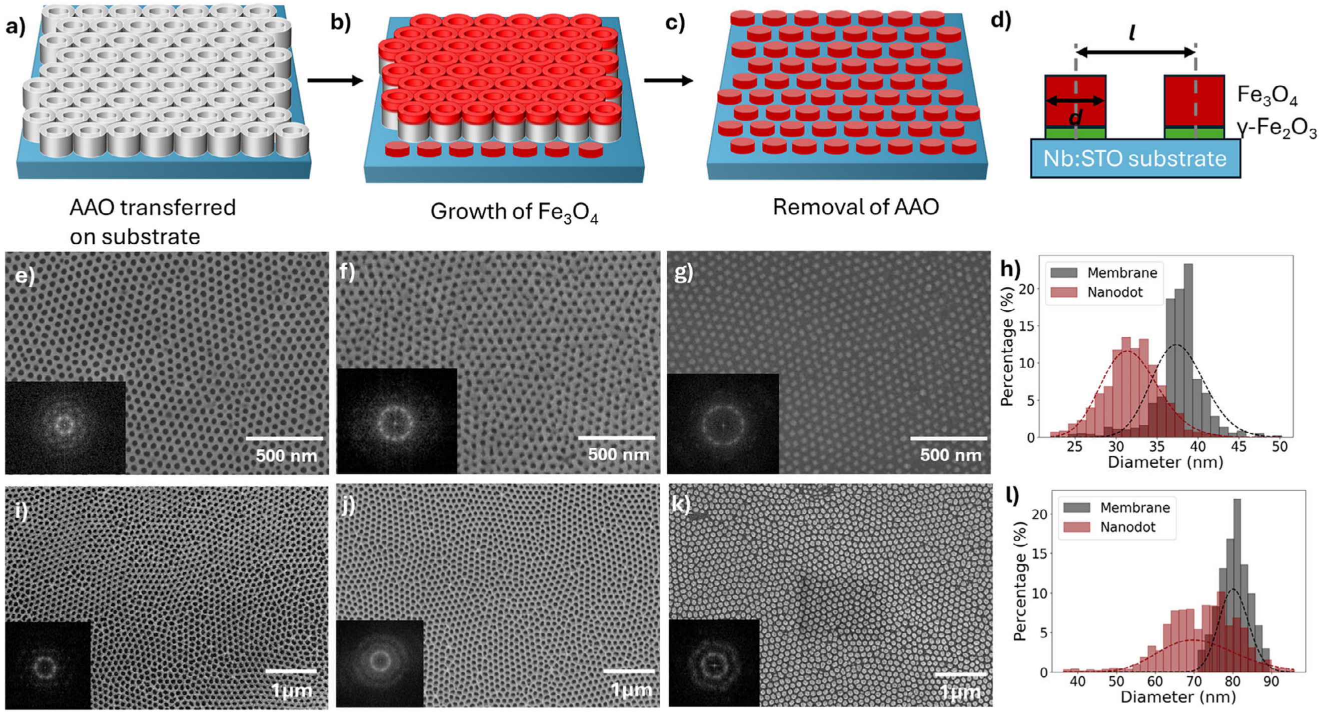

FIGURE 2 | Fabrication and SEM characterization of Fe_3O_4 nanodots on Nb:STO using AAO templates. (a–c) Schematic illustration of the fabrication steps: (a) AAO membrane on Nb:STO, (b) Fe_3O_4 deposition through the template, and (c) template removal, leaving ordered nanodots. (d) Schematic cross-section showing nanodot on the Nb:STO substrate. (e–g) SEM images of the 30 nm sample corresponding to steps (a–c), respectively. Insets show FFT patterns. (i–k) SEM images of the 70 nm sample corresponding to steps (a–c), respectively. Insets show FFT patterns. (h, l) Diameter distributions of nanopores (gray) and nanodots (red) extracted from (e, g) and (i, k), respectively, with log-normal fits (dashed lines).

The morphology of the samples at different fabrication stages was examined using SEM. Figure 2e shows a top-view SEM image of the 30 nm AAO/Nb:STO sample, revealing a well-ordered array of round pores. The inset shows the corresponding fast Fourier transform (FFT), which exhibits a sixfold symmetric pattern. This confirms the hexagonal ordering of the AAO template on the substrate. To assess uniformity, SEM images were acquired from multiple regions across the sample. These images consistently showed similar ordering, which supports the successful and uniform transfer of the AAO membrane onto the Nb:STO substrate.

Figure 2f shows an SEM image of the AAO/Nb:STO substrate after Fe_3O_4 deposition. The film was deposited using PLD, during which the AAO template acted as a physical mask. Figure 2g shows the resulting Fe_3O_4 nanodots after removing the AAO template. A close-up SEM image of both the membrane with the deposited film and the resulting nanodots is shown in Figure S5. The deposition was carried out under the same PLD parameters as used for continuous thin films, yielding nanodots with comparable thickness.

To examine the influence of Fe_3O_4 deposition on the array ordering, FFT patterns of the nanopores (Figure 2e), the pore structure after deposition (Figure 2f), and the resulting nanodots (Figure 2g) were compared. In all cases, distinct Bragg spots demonstrate that the hexagonal arrangement is preserved. The slight variations in intensity and spacing arise naturally from the transition between imaging pores, filled pores, and nanodots in addition to the growth process using the PLD. Overall, the nanostructure array retains its long-range order. SEM images also reveal rotational domains of the AAO template, which are transferred to the Fe_3O_4 nanodots and give rise to domain-like variations in the FFT pattern.

A histogram was used to quantify the size distribution of the nanostructures. Over 800 individual nanostructures within the SEM image were analyzed. The resulting distribution was fitted with a log-normal function, as shown in Figure 2h. The nanopores in the membrane have an average diameter of 37.7 nm ± 0.11 nm, the resulting nanodots have an average diameter that is slightly smaller at 31.7 nm ± 0.12 nm. Both follow a log-normal distribution. The small standard deviations indicate excellent size uniformity across the array. The reduction in size from pore to nanodot diameter can be attributed to the shadowing effect of the AAO template during deposition. This shadowing effect limits material deposition in the areas directly underneath the edges of the pore openings [58].

The same methodology was used for a 70 nm-pore-size AAO template (Figure 2i–k). The SEM and FFT analysis confirm that the hexagonal ordering is preserved, and that the nanodots have a regular shape and spacing. The size distribution (Figure 2l) follows a log-normal form again, albeit with a slightly reduced mean diameter compared to the pore size, which is consistent with the 30 nm sample. These results demonstrate that the fabrication method is reproducible across different template diameters.

Although the AAO-assisted fabrication of nanostructures has been studied previously for creating highly ordered nanodevices,

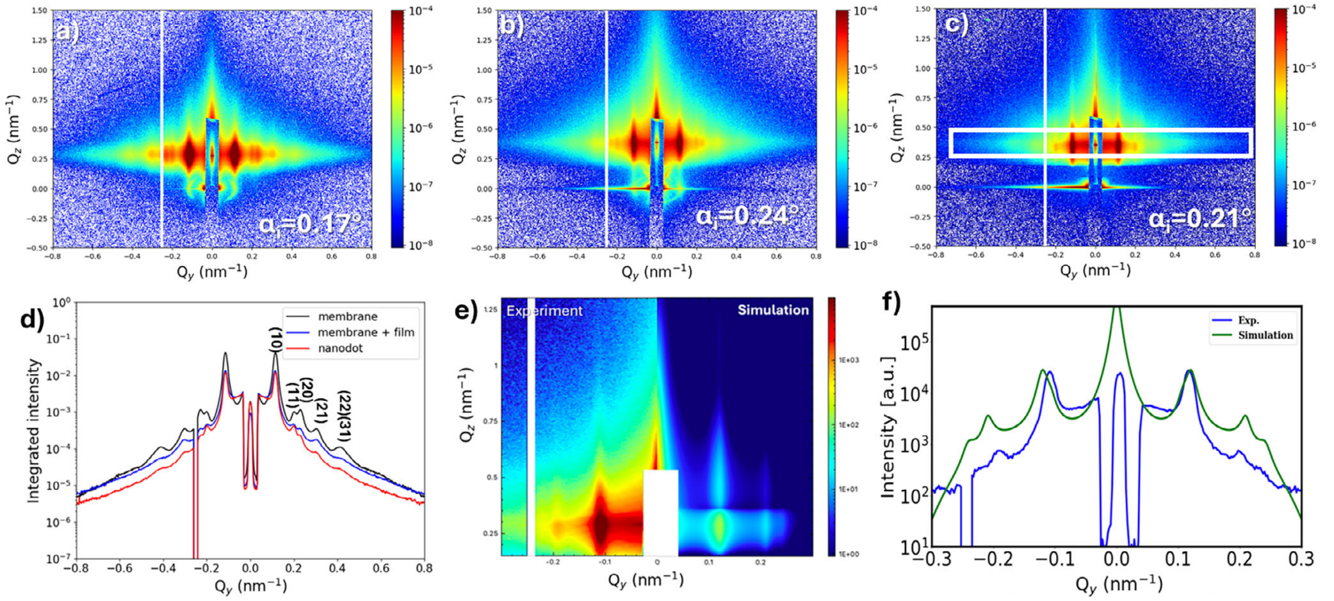

FIGURE 3 | GISAXS patterns of 30 nm nanostructures at different fabrication stages: (a) AAO/Nb:STO; (b) Fe_3O_4/AAO/Nb:STO; (c) Fe_3O_4/Nb:STO. (d) Integrated GISAXS intensity along Q_y for the three fabrication stages. The Bragg peaks are indexed assuming a 2D hexagonal lattice with an interpore/interdot distance of $l = 63.5 \pm 0.5$ nm. (e) Left: zoom-in of the experimental GISAXS pattern shown in (f); right: corresponding simulation. (f) Integrated intensity along Q_z from the experimental and simulated patterns shown in (h).

the majority of studies depend on characterization techniques that are very localized, such as SEM, TEM, or AFM [25, 26, 59]. These methods provide qualitative information limited to small areas, typically on the order of a few square microns. To overcome this limitation, we performed GISAXS measurements to probe nanostructures across larger areas of the substrate and gain further insights into the in-plane lateral ordering of the nanodots. In our setup, the illuminated area on the sample surface is approximately 0.7×0.7 mm ^{2}. This allows us to average structural information over an area several orders of magnitude larger than is typically accessible by SEM or TEM [60].

Figure 3a–c shows the GISAXS patterns corresponding to different fabrication stages of the 30 nm nanodots, which were measured at an incident angle of $\alpha_i \approx 0.2°$. Figure 3a shows the GISAXS patterns for the AAO/Nb:STO. The Bragg rods along Q_y, confirm that the hexagonal pore arrangement of the AAO template is preserved after transfer. Figure 3b shows the GISAXS patterns for Fe_3O_4/AAO/Nb:STO, where Bragg rods along Q_y remain, indicating that the Fe_3O_4 film conforms to the lateral ordering of the AAO template. Additionally, the slight sharpening of the rods along Q_z suggests that the deposited Fe_3O_4 film has a relatively consistent thickness profile over the template. Figure 3c shows the GISAXS patterns for Fe_3O_4/Nb:STO. An overall reduction in intensity is observed in this figure, which can be attributed to changes in form factor and contrast upon transformation from pores to nanodots after template removal. At the same time, the Q_z rods extend to higher Q values, indicating that the Fe_3O_4 nanodots are relatively uniform in height. This leads to enhanced vertical correlation in the scattering signal which is seen as more well-defined peaks in the GISAXS pattern.

The integrated intensity plot along Q_y (Figure 3d), around the Yoneda line (white box) reveals the periodicity is maintained throughout all fabrication stages, as seen in the GISAXS patterns (Figure 3a–c). The nanopores/nanodots are arranged in a hexagonal lattice geometry with an interpore/interdot distance $l = 63.5$ nm, extracted from the first-order Bragg peak. Further details are given in Section S6. This geometry yields an areal nanodot density on the order of 10^{10} cm $^{-2}$, placing it within the range of high-density device architectures reported in the literature [25, 61] (See details in Section S7). Additionally, the reduction in higher-order peak intensity indicates limited lateral order, which may be caused by surface roughness or incomplete coverage introduced during deposition and template removal, thereby decreasing the constructive interference. The Bragg peaks were indexed under the assumption of a 2D hexagonal lattice, and validation is provided in Section S6. GISAXS simulations of the 30 nm nanodot (Figure 3c) were performed using the BornAgain software based on the distorted-wave Born approximation (DWBA) to support the experimental findings [62]. The nanodots were modeled as truncated nanospheres arranged in a hexagonal lattice on Nb:STO (see Section S8 for details). The simulated pattern (Figure 3d) successfully reproduces the main features of the experimental data, including the discrete Bragg peaks arising from the lateral hexagonal ordering of the nanodots. In the integrated intensity plot (Figure 3f), the simulated data were scaled by a single global intensity factor to enable direct comparison. No structural parameters were adjusted, which underscores the robustness of the assumed dot geometry in the model. Detailed simulation parameters, modeling approach, and comparisons to experimental data are presented in Section S8.

GISAXS characterization of nanodots fabricated using the 70 nm AAO template is presented in Section S9. The additional GISAXS data confirm that long-range lateral ordering is also preserved at the larger dot diameter. The consistency across different template sizes demonstrates the robustness of the fabrication approach and provides a strong foundation for comparing their structure and

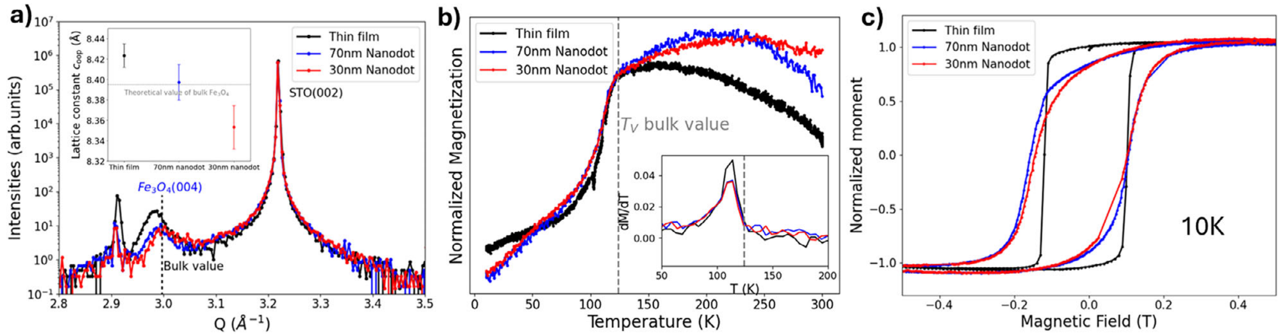

FIGURE 4 | Comparison between thin film and nanodot grown under identical conditions: (a) XRD patterns with the inset of calculated out-of-plane lattice constant c_{oop}; (b) Temperature-dependent magnetization, with the inset displaying the first derivative d M /d T; (c) Magnetic hysteresis loops measured at 10 K.

properties to those of the parent thin film and exploring their potential in nanoscale functional applications.

In summary, SEM and GISAXS demonstrate that the AAO-assisted method creates reproducible, long-range ordered Fe_3O_4 nanodot arrays across different template diameters. The resulting high-density arrangement can provide an important prerequisite for the integration of memristive arrays on a larger scale. This may enable enhanced storage capacity and scalability via nanostructure fabrication, thereby offering a robust platform for further structural, magnetic, and electrical investigations.

2.3 | Comparison of Structural and Magnetic Properties: Film Versus Nanodots

Significant variations in physical properties can occur when the dimensionality of a material is reduced from a thin film to nanoscale structures due to factors such as an increased surface-to-volume ratio, strain relaxation, or altered magnetic domain structures [63, 64]. We compared the crystallinity, stoichiometry, and magnetic response of the Fe_3O_4 nanodots to the continuous films to see if they preserve the essential structural and magnetic characteristics of the continuous films.

X-ray diffraction (XRD) was used to probe crystallinity. As shown in Figure 4a, the nanodots exhibit the same (001) diffraction peak as Fe_3O_4 thin films grown on Nb:STO (001) substrates, confirming that the out-of-plane crystallographic orientation is maintained. Using Bragg's law, the out-of-plane lattice constants c_{oop} were calculated to be 8.42 ± 0.01 Å for the thin film, 8.35 ± 0.02 Å for the 30 nm nanodots, and 8.40 ± 0.02 Å for the 70 nm nanodots. These values correspond to out-of-plane lattice constants averaged over many nanodots through their full thickness. Both nanodot samples have statistically similar values to the continuous thin film.

We then examined whether the nanodots chemically retain the magnetite phase by analyzing the Verwey transition, a well-known indicator of stoichiometric Fe_3O_4. The Verwey transition temperature, T_V, is a characteristic of magnetite and is highly sensitive to oxygen content, making it a useful probe to distinguish between Fe_3O_4 and overoxidized phases such as γ-Fe_2O_3. For $Fe_{3-\delta}O_4$, where $\delta > 0.036$, the Verwey transition is not detectable [65]. The value of T_V can be determined from zero-field-cooled magnetization measurements with an applied field of 500 Oe. As shown in Figure 4b, the magnetization as a function of temperature ($M(T)$) curves for both the thin film and (30 nm, 70 nm) nanodots with raw data shown in Section S10.

The Verwey transition temperature is extracted from the maximum of the first derivative of magnetization, $\partial M/\partial T$ as shown in the inset of Figure 4b. Both the thin film and the nanodots exhibit the Verwey transition at $T_V = 114$ K, indicating that all materials are near-stoichiometric. This value is slightly lower than the bulk Verwey transition temperature of $T_{V,\text{theo}} \approx 124$ K. This reduction can be attributed to several factors: (1) thickness effects, where reduced film thickness causes the formation of anti-phase boundaries (APBs) and lowers T_V [18, 66]; (2) lattice mismatch between Fe_3O_4 and STO (-7.5%) exacerbates APB formation [18, 67, 68]; and (3) slight stoichiometric variations in oxygen content, where slight deviations from stoichiometry can decrease T_V [69, 70]. The agreement in Verwey transition temperatures confirms that both the nanodots and the thin film have similar Fe_3O_4 stoichiometry. The width of the transition δT_V for the nanodots is 15 K, which is broader than the 10 K observed for the thin film. A broader Verwey transition has been observed in smaller nanostructures or thin films with multicrystalline domains [19, 71]. In our case, the broadening might also result from a distribution of domain sizes or the presence of grain boundaries within the nanodots, which can smear out the transition.

Hysteresis loops were measured using VSM to determine the coercivity (H_c) and remanent magnetization (M_r) of the Fe_3O_4 thin films and nanodots. Measurements were recorded at various temperatures and normalized as discussed in Section S11. In Figure 4c, the hysteresis loops at 10 K for the thin film, 70 nm nanodots, and 30 nm nanodots are compared. The shape of the loop evolves from a rectangular form in the thin film to an S-shaped loop in the nanodots. To quantify the magnetic anisotropy and ease of magnetization reversal, the squareness of the hysteresis loop, defined as the ratio M_R/M_S, was extracted. The squareness is found to be 0.85 ± 0.02 for the thin film, 0.61 ± 0.05 for the 70 nm nanodots, and 0.58 ± 0.04 for the 30 nm nanodots, averaged over the temperature range of 10–300 K. Given that both the nanodots and thin film have a similar thickness (≈30 nm), differences in behavior can be attributed primarily to geometry and interface effects rather than thickness effects. The observed reduction in squareness with decreasing dot diameter suggests a decrease in magnetic coherence across the array and is in line with the expected transition toward single-domain behavior within individual nanodots due to size confinement [72–74]. As the nanodot size approaches the critical single-domain dimension of Fe_3O_4 (approximately 80 nm [75]), magnetization reversal occurs predominantly by coherent rotation, resulting in the smoother, *S*-shaped hysteresis. While each nanodot can behave as a single magnetic domain, the overall array may still show variation in magnetization direction from dot to dot. In addition, when the nanodot volume is sufficiently large, dipolar interactions between neighboring dots become significant [76], which may also contribute to the gradual *S*-shaped reversal [76, 77].

In summary, although scaling down to nanodots leads to minor differences compared to the continuous film, such as a modified magnetic loop shape, the main structural and magnetic characteristics of the magnetite phase are well preserved. The nanodots retain the same crystallographic orientation as the parent Fe_3O_4 thin film, and remain stoichiometric and ferrimagnetic, making them suitable for further functional exploration.

2.4 | Resistive Switching in Thin Films and Nanodots

We investigated the electrical behavior of Fe_3O_4/Nb:STO heterostructures to explore their potential for resistive switching applications. Previous studies on this system have consistently reported rectifying current–voltage ($I-V$) characteristics, which were attributed to Schottky barrier formation at the interface. However, none of these studies demonstrated resistive switching behavior at room temperature or across the Verwey transition range [31, 32, 78, 79]. In most of those cases, the films were polycrystalline or grown to minimize interfacial oxidation and secondary phases, which may have limited their ability to induce or observe switching.

In contrast, the continuous epitaxial Fe_3O_4 layer in our system exhibits clear bipolar resistive switching, as shown in Figure 5a. The ($I-V$) curves from the Fe_3O_4 film on Nb:STO, which includes a thin γ-Fe_2O_3.interfacial layer, demonstrate a gradual transition between high and low resistance states. Stable behavior is observed over 100 consecutive switching cycles. Switching occurs without an abrupt forming step and is polarity-dependent, indicating a stable and forming-free bipolar switching behavior.

To evaluate the effects of scaling, we performed readouts at -0.3 V for different contact areas (2500–40000 μ m ^{2}) in the initial, low resistance state (LRS), and high resistance state (HRS). As shown in Figure 5b, the resistance in the initial state decreases with increasing area, with a slope of approximately −0.86 in the log–log plot. This is consistent with homogeneous conduction through the film. After switching, however, the resistance shows a stronger dependence on contact area, with fitted slopes of −2.34 (LRS) and −2.97 (HRS).

Having evidenced resistive switching behavior in the thin film, we next tested whether this behavior persists at the nanoscale by measuring *I–V* curves on individual nanodots. In this study, we focused on the 30 nm nanodot sample, which offers a higher degree of ordering, well-separated features, and a more pronounced nanoscale confinement effect than the 70 nm nanodot sample.

However, achieving reliable electrical contact with nanomaterials using conventional probe stations remains inherently challenging. We used conductive atomic force microscopy (C-AFM, Omicron VT SPM) to map morphology and conductivity simultaneously, enabling local electrical characterization of individual Fe_3O_4 nanodots. Figure 5c presents the topography, while Figure 5d shows the corresponding current map, acquired at a bias of +1V. The distinct arrangement of nanodots is consistent with the SEM and GISAXS observations. The current map reveals brighter intensity on the nanodots, while the Nb:STO substrate shows lower intensity, suggesting a higher current on the nanodots than that of the substrate [80]. To further analyze the correlation between topography and conductivity, the topography scan profile extracted from the blue line in Figure 5c is plotted together with the current profile extracted from the dashed orange line in Figure 5d, as shown in Figure 5e. The nanodot height ranges from 20 to 30 nm, with possible influence from tip–sample convolution, in agreement with XRR measurements (Section S16), while the current peaks fall between 100 and 150 nA. The current profile follows the same phase as the topography scan, confirming that the current is primarily dominated by the Fe_3O_4 nanodots.

To demonstrate the resistive switching of a single nanodot, additional electrical characterization was performed, as shown in Figure 5f. The ($I-V$) curve, averaged over three sweeps within ±2 V on the green dot in Figure 5c, is obtained with a current compliance of 10 nA to ensure tip stability. The results show SET behavior under negative voltage and RESET under positive voltage, i.e., by biasing the Fe_3O_4 nanodot to -2 V, the nanodot is set to a low resistance state (LRS), while a +2 V bias resets to a high resistance state (HRS). These results establish that the resistive switching behavior observed in the continuous film is preserved at the single-nanodot level. The ON/OFF resistance ratio in our Fe_3O_4/Nb:STO system is of the same order as that reported for other Fe_3O_4 based systems. A detailed comparison of reported ON/OFF ratios is provided in Section S13.

2.5 | Discussion of Resistive Switching in Fe_3O_4/γ-Fe_2O_3/Nb:STO

Based on the experimental observations, the resistive switching behavior of the thin film and nanodot structures may be rationalized in a qualitative manner. From the structural analysis, it was observed that a layered structure of a (half-metallic) Fe_3O_4 top layer and interfacial γ-Fe_2O_3 layer is established, forming a nanometer-thin insulating barrier close to the thin-film-to-substrate interface (Figure 6). Due to the good conductivity of the Fe_3O_4 top layer, it is expected that the applied potential mainly drops in this region, implying that the total resistance is determined by the insulating interfacial layer. Here, we note that we consistently observed ohmic contact between the Au top electrode and the Fe_3O_4 layer (details in Section S12) in the standard MIM structures, supporting that the switching process originates at the buried γ-Fe_2O_3 layer rather than at the film surface.

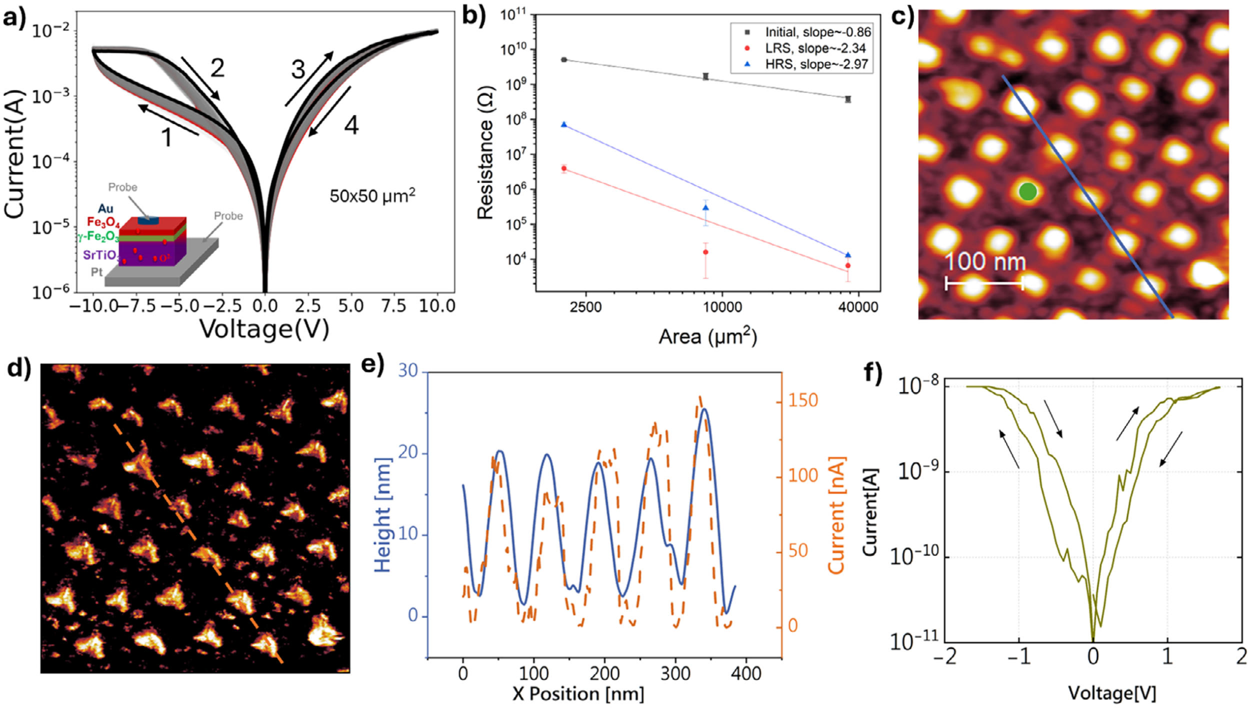

FIGURE 5 | (a) Current–voltage ($I-V$) characteristics over 100 cycles, (b) Area-dependence of resistance for initial states, LRS, and HRS plotted in log–log scale of a 30 nm-thick Fe_3O_4 film on Nb:STO; Conductive AFM measurement of the 30 nm-diameter Fe_3O_4 nanodots. (c) Topography of 400 nm by 400 nm area using 1nN force for scanning. (d) The current map acquired simultaneously with the topography (c) at a bias of +1 V. (e) Topography and current scan-profiles of the blue line in (c) and the dashed orange line in (d), showing the current response spatially fit to where the nanodots are. (f) $I–V$ sweep of the nanodot indicated by a green dot in (c).

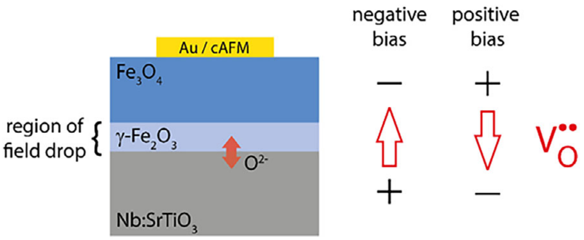

FIGURE 6 | Schematic illustration of the layered Fe_3O_4/γ-Fe_2O_3/Nb:STO structure, showing resistive switching behavior. The moving direction of oxygen (vacancies), $V_O^{\bullet\bullet}$, driven by the applied bias polarity, hints towards oxygen exchange across the Nb:STO/γ-Fe_2O_3 interface.

The switching polarity observed both in the MIM structures as well as in the cAFM-based nanodot experiments indicates a transition from high resistance state (HRS) to low resistance state (LRS) at negative polarity of the applied potential, while a positive bias results in a transition from LRS to HRS. Therefore, a negative applied potential apparently reduces the insulating γ-Fe_2O_3 layer toward more conductive Fe_3O_{4-x}, resulting in an overall lowered resistance (LRS). Based on the moving direction of oxygen (vacancies) under this bias, this may indicate that the switching is related to oxygen insertion from the γ-Fe_2O_3 layer into the Nb-doped substrate (i.e., oxygen (vacancies) moving downwards (upwards) in Figure 6).

In turn, positive polarity may reoxidize the interfacial layer toward the insulating γ-Fe_2O_3, thereby increasing the overall resistance (HRS). In this case, the moving direction of oxygen (vacancies) may indicate that oxygen is re-inserted from the substrate into the interfacial layer (i.e., oxygen (vacancies) moving upwards (downwards) in Figure 6). Based on this oxygen exchange, both the insulating γ-Fe_2O_3 layer as well as the resulting contact resistance to the Nb:STO substrate may be modulated, further contributing to the observed resistance change [81].

As an alternative scenario, one may consider a direct oxygen exchange between Fe_3O_4 top layer and the interfacial γ-Fe_2O_3 layer, potentially involving the reported topotactic phase transition between the two phases [82–84]. In this case, however, a negative bias would primarily reduce the conducting Fe_3O_4 layer (oxygen vacancies moving ‘upwards’), leading to an increased resistance, rather than the observed LRS, making this scenario less likely (or less pronounced).

Based on the cAFM measurements, it is indicated that at the nanoscale, each of the 30 nm-sized nanodots (Section S14 for 70 nm nanodots) may serve as an individual memristive device, as the resistive switching is preserved at the single-dot level, with bipolar SET/RESET transitions observed locally (Figure 5f). This offers the ability to reversibly switch single nanodots, underscoring the potential for using individual nanodots as addressable resistive switching units.

3 | Conclusion

We present a bottom-up approach to fabricate high-quality Fe_3O_4 thin films and nanodots on Nb:STO substrates. X-ray and neutron techniques suggest the formation of a thin interfacial layer of

γ-Fe_2O_3. The combination of pulsed laser deposition and AAO templating enable the growth of laterally confined nanodots with well-defined morphology and long-range ordering. Comprehensive structural and magnetic characterization shows that the nanodots preserve key features of the continuous film, including epitaxial quality and the Verwey transition, confirming that the essential properties of magnetite are maintained upon scaling. The successful transfer of film properties to nanoscale structures highlights the robustness of this fabrication method and its suitability for exploring correlated oxide systems in confined geometries. Local electrical measurements further establish that resistive switching persists down to individual 30 nm nanodots, demonstrating that single nanodots can act as memristive elements. This provides a solid basis for advancing functionality toward nanoscale memory arrays and for exploring additional coupled properties, such as magneto-electronic or spintronic effects, in confined geometries.

4 | Experimental Methods

4.1 | Deposition of Fe_3O_4 Thin Films

Fe_3O_4 thin films were deposited using pulsed laser deposition (PLD) with a rotating Fe_2O_3target. The Nb:STO substrate (Shinkosha Co., Ltd.) was pretreated to obtain TiO_2-termination prior to deposition (details in Section S1) and kept at a temperature of 450 ° C during deposition. The oxygen background pressure was set to 2×10^{-6} mbar, with a base pressure of 1×10^{-7} mbar. The laser fluence was set to $1.5\ J \cdot Cm^{-2}$, and the repetition rate was 5 Hz. To ensure uniform deposition, the target was aligned directly in front of the heater during deposition. A deposition time of 16 min at these parameters results in a 30 nm thick film.

4.2 | Fabrication of Fe_3O_4 Nanodots

Fe_3O_4 nanodots were fabricated on $10 \times 10 \times 0.5\ mm^3$ Nb:STO substrates using anodic aluminum oxide (AAO) templates as physical masks, as illustrated in Figure 2. Commercial AAO membranes (Shenzhen Topmembranes Technology Co., Ltd.) with nominal pore diameters of ≈30 or ≈ 70 nm, interpore distances of ≈ 65 or ≈125 nm, and a thickness of 100 nm were precoated with a PMMA support layer to aid transfer. The templates were transferred onto the substrates (see Section S15 for details), and Fe_3O_4 was deposited via PLD using the same parameters as for the continuous film. After deposition, the templates were removed using Kapton tape, resulting in a well-ordered nanodot array.

X-ray reflectivity measurements (XRR) confirmed that the nanodots have a thickness of approximately 30 nm, comparable to the thin film grown under identical conditions (detailed in Section S16).

4.3 | Characterization Techniques

X-ray reflectivity measurements (XRR) and X-ray diffraction (XRD) measurements were carried out on both Fe_3O_4 thin films and nanodot samples using a Bruker D8 diffractometer with Cu K_α radiation to obtain crystallographic information and phase purity. Scanning electron microscopy (SEM, Hitachi SU8000) and grazing incidence small-angle X-ray scattering (GISAXS) were used specifically on the nanodot samples to examine their surface morphology, spatial distribution, and long-range ordering. GISAXS measurements were carried out using the Gallium Anode Low-Angle X-ray Instrument (GALAXI) with a monochromatic X-ray beam of $\lambda = 0.13414$ nm [85].

A TEM cross-section of the thin film sample was prepared with a Thermo Fisher Scientific FEI Scios Dual Beam FIB/SEM system. 2 keV was used for final polishing of the TEM lamellae to minimize surface damage. The TEM study was performed at a probe corrected Thermo Scientific Titan at 300 kV equipped with a high-performance super-X energy-dispersive X-ray spectroscopy (EDS) system, which was used to map the elemental distribution. The EELS spectra were acquired at the same TEM, using the Gatan Imaging Filter (GIF Quantum).

The magnetic properties of both the thin film and nanodots were investigated using a vibrating sample magnetometer (VSM) within a Quantum Design Physical Properties Measurement System (PPMS-Dynacool). Temperature-dependent magnetization, $M(T)$, was measured under zero-field cooling (ZFC) conditions with an applied magnetic field of 500 Oe. Hysteresis loops were recorded at room temperature under an applied magnetic field of ±2 T along the in-plane [100] axis.

X-ray absorption spectroscopy (XAS) and X-ray magnetic circular dichroism (XMCD) measurements were conducted on the thin film at the DEIMOS beamline at SOLEIL [86], with magnetic fields of ±2 T applied. Measurements were taken using both circular right (CR) and circular left (CL) polarized light, and detected in total electron yield (TEY) mode.

Polarized neutron reflectometry (PNR) measurements were performed on the thin film at room temperature with an applied in plane field of 0.7 T at the D17 beamline at ILL [87].

Current–voltage (I–V) measurements were performed on the thin film using a Keithley 2611A source measurement unit and a PM5 probe station with two micromanipulators. Gold top electrodes with varying contact areas were deposited through a shadow mask and contacted using a gold coated tungsten needle. The Nb:STO substrates, serving as bottom electrodes, were mounted on Pt-coated Si wafers using silver paint to ensure good electrical contact. I–V sweeps of the Keithley 2611A were typically conducted with a voltage step size of 30 mV s^{-1} and a delay time of 20 ms between steps.

Morphological and electrical characterizations of the nanodots were carried out using conductive atomic force microscopy (cAFM) with an Omicron VT Scanning Probe Microscope (VT-SPM) at room temperature. Super-sharp conductive single-crystal diamond probes (Bruker AD-2.8-SS) were employed for both topographic imaging and single-point I–V measurements. The nominal apex radius of the conductive diamond tip was less than 5 nm. To prevent tip damage from excessive current, a current compliance was applied via the sourcemeter Keithley 2401.

Acknowledgements

The authors gratefully acknowledged Emmanuel Kentzinger, Ulrich Rücker, and Steffen Tober for their support with the GISAXS measurements using the GALAXI setup at JCNS-2, Forschungszentrum Jülich, including assistance during the experiments and helpful discussions. The authors would like to thank Sylvia de Waal, Grigory Potemkin, Anton Kaus, and Vitor Alexandre de Oliveira Lima for etching the substrate. The authors are grateful to Mathias Getzlaff for his support and the insightful input he shared with us. The author acknowledged SOLEIL for the provision of synchrotron radiation facilities and the authors acknowledged the provision of beamtime on the D17 instruments at the Institute Laue-Langevin (https://10.5291/ILL-DATA.5-54-402). The authors would like to thank Hebatalla Elnaggar for the assistance in analyzing the XMCD data. The authors also thank Karen Friese for supporting this project, and Thomas Brückel for his encouragement and for enabling the framework that made this work possible at JCNS-2.

Open access funding enabled and organized by Projekt DEAL.

Conflicts of Interest

The authors declare no conflicts of interest.

Data Availability Statement

The data that support the findings of this study are available from the corresponding author upon reasonable request.

References

1. M. Bibes and A. Barthelemy, "Oxide Spintronics," *IEEE Transactions on Electron Devices* 54, no. 5 (2007): 1003–1023.

2. P. A. Cox, *Transition Metal Oxides: An Introduction to Their Electronic Structure and Properties*, 27 (Oxford University Press, 2010).

3. D. Panda and T.-Y. Tseng, "Perovskite Oxides as Resistive Switching Memories: A Review," *Ferroelectrics* 471, no. 1 (2014): 23–64.

4. M. Mejia-Santillan, N. Pariona, J. Bravo-C, et al., "Physical and Arsenic Adsorption Properties of Maghemite and Magnetite Sub-Microparticles," *Journal of Magnetism and Magnetic Materials* 451 (2018): 594–601.

5. C.-H. Shih, L. Chang, W.-L. Wang, and K.-K. Wang, "Revisiting the Phase Transformations of Wüstite Scale Formed on Low Carbon Steel," *Scripta Materialia* 262 (2025): 116657.

6. M. Capra, A. Lodesani, A. Brambilla, et al., "Reversible Metamorphosis from Fe_3O_4 to FeO of Epitaxial Iron Oxide Films Grown on the Fe-P(1×1)O Surface," *RSC Advances* 11, no. 19 (2021): 11513–11518.

7. K. Yamada, S. Tobashi, and S. Ichiba, "Topotactic Oxidation Process from Magnetite to Maghemite Studied by Rietveld Analysis and ^{119}Sn Mössbauer Spectroscopy," *Chemistry Letters* 8 (1990): 1327–1330.

8. M. H. Hamed, Y. Xu, H. Elnaggar, M. Zaghloul, A. M. Mio, A. Backs, A. Stellhorn, V. de O. Lima, C. Yin, C. Bednarski-Meinke, N. Steinke, O. Petracic, T. Brückel, T. Saerbeck, and A. Qdemat, "Magnetic Domain Texture in Fe_3O_4 Thin Films on SiO_2 Nanospheres," *Advanced Materials* (2025), https://doi.org/10.1002/adma.202513849.

9. M. Oku and K. Hirokawa, "X-Ray Photoelectron Spectroscopy of Co_3O_4, Fe_3O_4, Mn_3O_4, and Related Compounds," *Journal of Electron Spectroscopy and Related Phenomena* 8, no. 5 (1976): 475–481.

10. A. S. Teja and P.-Y. Koh, "Synthesis, Properties, and Applications of Magnetic Iron Oxide Nanoparticles," *Progress in Crystal Growth and Characterization of Materials* 55, no. 1–2 (2009): 22–45.

11. G. S. Parkinson, "Iron Oxide Surfaces," *Surface Science Reports* 71, no. 1 (2016): 272–365.

12. Z. Cvejic, S. Rakic, A. Kremenovic, B. Antic, C. Jovalekic, and P. Colomban, "Nanosize Ferrites Obtained by Ball Milling: Crystal Structure, Cation Distribution, Size-Strain Analysis and Raman Investigations," *Solid State Sciences* 8, no. 8 (2006): 908–915.

13. S. Yamauchi, M. Hibino, and T. Yao, "Structure Change Analysis in γ-Fe_2O_3/Carbon Composite in the Process of Electrochemical Lithium Insertion," *Solid State Ionics* 191, no. 1 (2011): 45–48.

14. V. R. Nallagatla, T. Heisig, C. Baeumer, et al., "Topotactic Phase Transition Driving Memristive Behavior," *Advanced Materials* 31, no. 40 (2019): 1903391.

15. A. Khare, D. Shin, T. S. Yoo, et al., "Topotactic Metal–Insulator Transition in Epitaxial $SrFeO_x$ Thin Films," *Advanced Materials* 29, no. 37 (2017): 1606566.

16. S. Barth, S. Estrade, F. Hernandez-Ramirez, et al., "Studies on Surface Facets and Chemical Composition of Vapor-Grown One-Dimensional Magnetite Nanostructures," *Crystal Growth and Design* 9, no. 2 (2009): 1077–1081.

17. F. Liu, P. Cao, H. Zhang, et al., "Novel Nanopyramid Arrays of Magnetite," *Advanced Materials* 17, no. 15 (2005): 1893–1897.

18. X. Liu, A. Rata, C. Chang, A. Komarek, and L. Tjeng, "Verwey Transition in Fe_3O_4 Thin Films: Influence of Oxygen Stoichiometry and Substrate-Induced Microstructure," *Physical Review B* 90, no. 12 (2014): 125142.

19. J. Lee, S. G. Kwon, J.-G. Park, and T. Hyeon, "Size Dependence of Metal–Insulator Transition in Stoichiometric Fe_3O_4 Nanocrystals," *Nano Letters* 15, no. 7 (2015): 4337–4342.

20. I. Castellanos-Rubio, O. Arriortua, D. Iglesias-Rojas, et al., "A Milestone in the Chemical Synthesis of Fe_3O_4 Nanoparticles: Unreported Bulklike Properties Lead to a Remarkable Magnetic Hyperthermia," *Chemistry of Materials* 33, no. 22 (2021): 8693–8704.

21. L. An, Z. Li, W. Li, et al., "Patterned Magnetite Films Prepared via Soft Lithography and Thermal Decomposition," *Journal of Magnetism and Magnetic Materials* 303, no. 1 (2006): 127–130.

22. T. Nakanishi, Y. Masuda, and K. Koumoto, "Site-Selective Deposition of Magnetite Particulate Thin Films on Patterned Self-Assembled Monolayers," *Chemistry of Materials* 16, no. 18 (2004): 3484–3488.

23. H. Zhao, M. Zhou, L. Wen, and Y. Lei, "Template-Directed Construction of Nanostructure Arrays for Highly-Efficient Energy Storage and Conversion," *Nano Energy* 13 (2015): 790–813.

24. H. Masuda and K. Fukuda, "Ordered Metal Nanohole Arrays Made by a Two-Step Replication of Honeycomb Structures of Anodic Alumina," *Science* 268, no. 5216 (1995): 1466–1468.

25. J.-M. Song and J.-S. Lee, "Self-Assembled Nanostructured Resistive Switching Memory Devices Fabricated by Templated Bottom-Up Growth," *Scientific Reports* 6, no. 1 (2016): 18967.

26. M. A. Kashi and A. Montazer, "Template-Based Electrodeposited Nonmagnetic and Magnetic Metal Nanowire Arrays as Building Blocks of Future Nanoscale Applications," *Journal of Physics D: Applied Physics* 55, no. 23 (2022): 233002.

27. M.-B. Lepetit, B. Mercey, and C. Simon, "Interface Effects in Perovskite Thin Films," *Physical Review Letters* 108, no. 8 (2012): 087202.

28. F. V. Hensling, C. Baeumer, M.-A. Rose, F. Gunkel, and R. Dittmann, "$SrTiO_3$ Termination Control: A Method to Tailor the Oxygen Exchange Kinetics," *Materials Research Letters* 8, no. 1 (2020): 31–40.

29. M. Andrä, H. Bluhm, R. Dittmann, et al., "Chemical Control of the Electrical Surface Properties in Donor-Doped Transition Metal Oxides," *Physical Review Materials* 3, no. 4 (2019): 044604.

30. M. Andrä, C. Funck, N. Raab, et al., "Effect of Cationic Interface Defects on Band Alignment and Contact Resistance in Metal/Oxide Heterojunctions," *Advanced Electronic Materials* 6, no. 1 (2020): 1900808.

31. B. Carvello and L. Ranno, "Transport Properties of the Fe_3O_4/Nb:$SrTiO_3$ Interface," *Journal of Magnetism and Magnetic Materials* 272 (2004): 1926–1927.

32. D. C. Kundaliya, S. Ogale, L. Fu, et al., "Interfacial Characteristics of the Fe_3O_4/Nb (0.5%):$SrTiO_3$ Oxide Junction," *Journal of Applied Physics* 99, no. 8 (2006): 08K304.

33. J.-H. Lee, J. Luo, H. K. Choi, S.-T. D. Chueng, K.-B. Lee, and J.-W. Choi, "Functional Nanoarrays for Investigating Stem Cell Fate and Function," *Nanoscale* 12, no. 17 (2020): 9306–9326.

34. G. Tian, D. Chen, J. Yao, et al., "$BiFeO_3$ Nanorings Synthesized via AAO Template-Assisted Pulsed Laser Deposition and Ion Beam Etching," *RSC Advances* 7, no. 65 (2017): 41210–41216.

35. H. Han, K. Lee, W. Lee, M. Alexe, D. Hesse, and S. Baik, "Fabrication of Epitaxial Nanostructured Ferroelectrics and Investigation of Their Domain Structures," *Journal of Materials Science* 44 (2009): 5167–5181.

36. Z. Yao, C. Wang, Y. Li, and N.-Y. Kim, "AAO-Assisted Synthesis of Highly Ordered, Large-Scale TiO_2 Nanowire Arrays via Sputtering and Atomic Layer Deposition," *Nanoscale Research Letters* 10 (2015): 1–7.

37. Q.-X. Zhu, M. Zheng, M.-M. Yang, et al., "Interface-Correlated Exchange Bias Effect in Epitaxial Fe_3O_4 Thin Films Grown on $SrTiO_3$ Substrates," *Applied Physics Letters* 105, no. 24 (2014): 241604.

38. M. H. Hamed, R. A. Hinz, P. Lomker, et al., "Tunable Magnetic Phases at Fe_3O_4/$SrTiO_3$ Oxide Interfaces," *ACS Applied Materials & Interfaces* 11, no. 7 (2019): 7576–7583.

39. K. P. McKenna, F. Hofer, D. Gilks, et al., "Atomic-Scale Structure and Properties of Highly Stable Antiphase Boundary Defects in Fe_3O_4," *Nature Communications* 5, no. 1 (2014): 5740.

40. J. F. Bobo, D. Basso, E. Snoeck, et al., "Magnetic Behavior and Role of the Antiphase Boundaries in Fe_3O_4 Epitaxial Films Sputtered on MgO (001)," *The European Physical Journal B: Condensed Matter and Complex Systems* 24, no. 1 (2001): 43–49.

41. D. B. Williams and C. B. Carter, "Transmission Electron Microscopy," *Systematic Materials Analysis* 4 (1978): 407–432.

42. C. Colliex, T. Manoubi, and C. Ortiz, "Electron-Energy-Loss Spectroscopy Near-Edge Fine Structures in the Iron–Oxygen System," *Physical Review B* 44, no. 20 (1991): 11402.

43. C. Wang, D. R. Baer, J. E. Amonette, M. H. Engelhard, J. Antony, and Y. Qiang, "Morphology and Electronic Structure of the Oxide Shell on the Surface of Iron Nanoparticles," *Journal of the American Chemical Society* 131, no. 25 (2009): 8824–8832.

44. T. Manoubi, M. Tencé, and C. Colliex, "Quantification of White Lines in Electron Energy-Loss Spectroscopy (EELS)," *Ultramicroscopy* 28, no. 1–4 (1989): 49–55.

45. T. Pohlmann, T. Kuschel, J. Rodewald, et al., "Cation- and Lattice-Site-Selective Magnetic Depth Profiles of Ultrathin Fe_3O_4 (001) Films," *Physical Review B* 102, no. 22 (2020): 220411.

46. E. Pellegrain, M. Hagelstein, S. Doyle, et al., "Characterization of Nanocrystalline γ-Fe_2O_3 with Synchrotron Radiation Techniques," *Physica Status Solidi (B)* 215, no. 1 (1999): 797–801.

47. E. Stavitski and F. M. De Groot, "The CTM4XAS Program for EELS and XAS Spectral Shape Analysis of Transition-Metal L Edges," *Micron* 41, no. 7 (2010): 687–694.

48. R. A. Pattrick, G. Van Der Laan, C. M. B. Henderson, P. Kuiper, E. Dudzik, and D. J. Vaughan, "Cation Site Occupancy in Spinel Ferrites Studied by X-Ray Magnetic Circular Dichroism: Developing a Method for Mineralogists," *European Journal of Mineralogy* 14, no. 6 (2002): 1095–1102.

49. F. Schedin, E. Hill, G. Van der Laan, and G. Thornton, "Magnetic Properties of Stoichiometric and Nonstoichiometric Ultrathin Fe_3O_4 (111) Films on Al_2O_3 (0001)," *Journal of Applied Physics* 96, no. 2 (2004): 1165–1169.

50. L. Cao, O. Petracic, P. Zakalek, et al., "Reversible Control of Physical Properties via an Oxygen-Vacancy-Driven Topotactic Transition in Epitaxial $La_{\{0.7\}}Sr_{\{0.3\}}MnO_{3\text{-}\delta}$ Thin Films," *Advanced Materials* 31, no. 7 (2019): 1806183.

51. S. He, O. Petracic, V. Lauter, et al., "$La_{\{0.6\}}Sr_{\{0.4\}}CoO_{3\text{-}\delta}$ Films under Deoxygenation: Magnetic and Electronic Transitions Are Apart from the Structural Phase Transition," *Advanced Functional Materials* 34, no. 24 (2024): 2313208.

52. A. Glavic and M. Björck, "GenX 3: The Latest Generation of an Established Tool," *Journal of Applied Crystallography* 55, no. 4 (2022): 1063–1071.

53. P. Weiss and R. Forrer, "La Saturation Absolue des Ferromagnétiques et les Lois d'Approche en Fonction du Champ et de la Température," *in Annales de Physique* 10 (1929): 279–372.

54. H. Li, M. Kobayashi, S. Kou, et al., "Noncollinear Magnetism in Fe_3O_4 Induced via Site-Selective Rare-Earth Substitution Boosting Its Saturation Magnetization," *Small* 21, no. 13 (2025): 2411133.

55. W. Liu, Y. Xu, P. Wong, et al., "Spin and Orbital Moments of Nanoscale Fe_3O_4 Epitaxial Thin Film on MgO/GaAs (100)," *Applied Physics Letters* 104, no. 14 (2014): 142407.

56. W. Ren and L. Bellaiche, "Size Effects in Multiferroic $BiFeO_3$ Nanodots: A First-Principles-Based Study," *Physical Review B: Condensed Matter and Materials Physics* 82, no. 11 (2010): 113403.

57. D. Paramanik, S. Sahoo, S. Majumder, P. S. Raman, and S. Varma, "Size-Dependent Electronic Structure from InP Nano-Dots," *Vacuum* 84, no. 5 (2009): 602–606.

58. Q. Hao, H. Huang, X. Fan, et al., "Facile Design of Ultra-Thin Anodic Aluminum Oxide Membranes for the Fabrication of Plasmonic Nanoarrays," *Nanotechnology* 28, no. 10 (2017): 105301.

59. X.-F. Guan, D. Chen, Z.-Y. Quan, et al., "Morphology and Magnetic Properties of Fe_3O_4 Nanodot Arrays Using Template-Assisted Epitaxial Growth," *Nanoscale Research Letters* 10 (2015): 1–6.

60. A. Qdemat, E. Kentzinger, J. Buitenhuis, U. Rücker, M. Ganeva, and T. Brückel, "Self-Assembled Monolayer of Silica Nanoparticles with Improved Order by Drop Casting," *RSC Advances* 10, no. 31 (2020): 18339–18347.

61. J. Frascaroli, S. Brivio, F. F. Lupi, et al., "Resistive Switching in High-Density Nanodevices Fabricated by Block Copolymer Self-Assembly," *ACS Nano* 9, no. 3 (2015): 2518–2529.

62. G. Pospelov, W. Van Herck, J. Burle, et al., "BornAgain: Software for Simulating and Fitting Grazing-Incidence Small-Angle Scattering," *Journal of Applied Crystallography* 53, no. 1 (2020): 262–276.

63. S. Sun, C. B. Murray, D. Weller, L. Folks, and A. Moser, "Monodisperse FePt Nanoparticles and Ferromagnetic FePt Nanocrystal Superlattices," *Science* 287, no. 5460 (2000): 1989–1992.

64. Q. Jiang and X. Lang, "Size Dependence of Structures and Properties of Magnetic Materials," *The Open Nanoscience Journal* 1, no. 28 (2007): 32–59.

65. Z. Kakol, J. Sabol, J. Stickler, and J. Honig, "Effect of Low-Level Titanium (IV) Doping on the Resistivity of Magnetite near the Verwey Transition," *Physical Review B* 46, no. 4 (1992): 1975–1978.

66. S. Alraddadi, W. Hines, T. Yilmaz, G. Gu, and B. Sinkovic, "Structural Phase Diagram for Ultra-Thin Epitaxial Fe_3O_4/MgO (001) Films: Thickness and Oxygen Pressure Dependence," *Journal of Physics: Condensed Matter* 28, no. 11 (2016): 115402.

67. J. Dho, B.-G. Kim, and S. Ki, "Distinctive Uniaxial Magnetic Anisotropy and Positive Magnetoresistance in (110)-Oriented Fe_3O_4 Films," *Journal of Applied Physics* 117, no. 16 (2015): 163904.

68. M. B. Yazdi, M. Major, A. Wildes, et al., "Possible Evidence for a Spin-State Crossover in the Verwey State in Fe_3O_4 Thin Films," *Physical Review B* 93, no. 1 (2016): 014439.

69. F. Walz, "The Verwey Transition–A Topical Review," *Journal of Physics: Condensed Matter* 14, no. 12 (2002): R285.

70. R. Aragón, D. J. Buttrey, J. P. Shepherd, and J. M. Honig, "Influence of Nonstoichiometry on the Verwey Transition," *Physical Review B* 31, no. 1 (1985): 430–436.

71. X. Liu, C.-F. Chang, A. D. Rata, A. C. Komarek, and L. H. Tjeng, "Fe_3O_4 Thin Films: Controlling and Manipulating an Elusive Quantum Material," *npj Quantum Materials* 1, no. 1 (2016): 1–5.

72. R. Skomski, "Nanomagnetics," *Journal of Physics: Condensed Matter* 15, no. 20 (2003): R841.

73. B. D. Cullity and C. D. Graham, *Introduction to Magnetic Materials* (John Wiley & Sons, 2011).

74. V. I. Shubayev, T. R. Pisanic II, and S. Jin, "Magnetic Nanoparticles for Theragnostics," *Advanced Drug Delivery Reviews* 61, no. 6 (2009): 467–477.

75. Q. Li, C. W. Kartikowati, S. Horie, T. Ogi, T. Iwaki, and K. Okuyama, "Correlation between Particle Size/Domain Structure and Magnetic Properties of Highly Crystalline Fe_3O_4 Nanoparticles," *Scientific Reports* 7, no. 1 (2017): 9894.

76. D. Xue and Z. Yan, "Hysteresis of Hexagonal Arrays of Magnetic Nanodots," *Journal of Applied Physics* 100, no. 10 (2006).

77. C. Xu, Y. Ma, and P. Hui, "Equilibrium Magnetic Moment Configurations in Magnetic Nanoparticle Films: Effects of Anisotropy, Dipolar Interaction, and Zeeman Energy," *Journal of Applied Physics* 98, no. 8 (2005).

78. K. Yang, D. Kim, and J. Dho, "Schottky Barrier Effect on the Electrical Properties of Fe_3O_4/ZnO and Fe_3O_4/Nb: $SrTiO_3$ Heterostructures," *Journal of Physics D: Applied Physics* 44, no. 35 (2011): 355301.

79. M. Ziese, U. Köhler, R. Höhne, A. Bollero, and P. Esquinazi, "Schottky Barrier Formation at the Fe_3O_4/Nb: $SrTiO_3$ Interface," *Journal of Magnetism and Magnetic Materials* 290 (2005): 1116–1119.

80. M. Andrä, F. Dvořák, M. Vorokhta, et al., "Oxygen Partial Pressure Dependence of Surface Space Charge Formation in Donor-Doped $SrTiO_3$," *APL Materials* 5, no. 5 (2017): 056106.

81. C. Baeumer, N. Raab, T. Menke, et al., "Verification of Redox Processes as Switching and Retention Failure Mechanisms in Nb: $SrTiO_3$/Metal Devices," *Nanoscale* 8, no. 29 (2016): 13967–13975.

82. A. Odagawa, Y. Katoh, Y. Kanzawa, et al., "Electroforming and Resistance-Switching Mechanism in a Magnetite Thin Film," *Applied Physics Letters* 91, no. 13 (2007): 133503.

83. T. Ishibe, Y. Maeda, T. Terada, et al., "Resistive Switching Memory Performance in Oxide Hetero-Nanocrystals with Well-Controlled Interfaces," *Science and Technology of Advanced Materials* 21, no. 1 (2020): 195–204.

84. S. Muraoka, K. Osano, Y. Kanzawa, et al., "Fast Switching and Long Retention Fe–O ReRAM and Its Switching Mechanism," in *2007 IEEE International Electron Devices Meeting* (2007), 779–782.

85. E. Kentzinger, M. Krutyeva, and U. Rücker, "GALAXI: Gallium Anode Low-Angle X-Ray Instrument," *Journal of Large-Scale Research Facilities (JLSRF)* 2 (2016): A61–A61.

86. P. Ohresser, E. Otero, F. Choueikani, et al., "DEIMOS: A Beamline Dedicated to Dichroism Measurements in the 350–2500 eV Energy Range," *Review of Scientific Instruments* 85, no. 1 (2014): 013106.

87. T. Saerbeck, R. Cubitt, A. Wildes, G. Manzin, K. H. Andersen, and P. Gutfreund, "Recent Upgrades of the Neutron Reflectometer D17 at ILL," *Journal of Applied Crystallography* 51, no. 2 (2018): 249–256.

Supporting Information

Additional supporting information can be found online in the Supporting Information section.

Supporting File: adma71914-sup-0001-SuppMat.pdf.